This article has been accepted for publication in Monthly Notices of the Royal Astronomical Society *©: 2021 The Authors. Published by Oxford University Press on behalf of the Royal Astronomical Society. All rights reserved.*

Monthly Notices of the ROYAL ASTRONOMICAL SOCIETY

MNRAS **504,** 393–405 (2021) doi:10.1093/mnras/stab808
Advance Access publication 2021 March 22

An *XMM–Newton* study of active–inactive galaxy pairs

Matteo Guainazzi [1]★ Alessandra De Rosa [2] Stefano Bianchi [3] Bernd Husemann [4] Tamara Bogdanovic,[5] Stefanie Komossa,[6] Nora Loiseau,[7] Zsolt Paragi [8] Miguel Pérez-Torres,[9] Enrico Piconcelli[10] and Cristian Vignali [11]

[1] *ESA European Space Research and Technology Centre (ESTEC), Keplerlaan 1, NL-2201 AZ Noordwijk, the Netherlands*
[2] *INAF – Istituto di Astrofisica e Planetologia Spaziali (IAPS), via Fosso del Cavaliere, I-133 Roma, Italy*
[3] *Dipartimento di Matematica e Fisica, Università degli Studi Roma Tre, via della Vasca Navale 84, I-00146 Roma, Italy*
[4] *Max Planck Institute for Astronomy, Königstuhl 17, D-69117 Heidelberg, Germany*
[5] *Center for Relativistic Astrophysics, School of Physics, Georgia Institute of Technology, 837 State Street, Atlanta, GA 30332-0430, USA*
[6] *Max-Planck-Institut für Radioastronomie, Auf dem Hügel 69, D-521 Bonn, Germany*
[7] *ESA – European Space Astronomy Centre (ESAC), E-28692 Villanueva de la Cañada, Madrid, Spain*
[8] *Joint Institute for VLBI ERIC, Oude Hoogeveensedijk 4, NL-7991 PD Dwingeloo, the Netherlands*
[9] *Instituto de Astrofísica de Andalucía (IAA-CSIC), Glorieta de la Astronomía s/n, E-18008 Granada, Spain*
[10] *Osservatorio Astronomico di Roma (INAF), via Frascati 33, I-00040 Monte Porzio Catone, Roma, Italy*
[11] *Dipartimento di Fisica e Astronomia, Alma Mater Studiorum, Università degli Studi di Bologna, Via Gobetti 93/2, I-40129 Bologna, Italy*

Accepted 2021 March 15. Received 2021 March 1; in original form 2020 December 10

ABSTRACT

While theory and simulations indicate that galaxy mergers play an important role in the cosmological evolution of accreting black holes and their host galaxies, samples of active galactic nuclei (AGNs) in galaxies at close separations are still small. In order to increase the sample of AGN pairs, we undertook an archival project to investigate the X-ray properties of an SDSS-selected sample of 32 galaxy pairs with separations ≤150 kpc containing one optically identified AGN, which were serendipitously observed by *XMM–Newton*. We discovered only one X-ray counterpart among the optically classified non-active galaxies, with a weak X-ray luminosity ($\simeq 5 \times 10^{41}$ erg s^{-1}). 59 per cent (19 out of 32) of the AGNs in our galaxy pair sample exhibit an X-ray counterpart, covering a wide range in absorption-corrected X-ray luminosity (5×10^{41}–2×10^{44} erg s^{-1}). More than 79 per cent of these AGNs are obscured (column density $N_{\rm H} > 10^{22}$ cm^{-2}), with more than half thereof (i.e. about 47 per cent of the total AGN sample) being Compton-thick. AGN/no-AGN pairs are therefore more frequently X-ray obscured (by a factor ≃1.5) than isolated AGNs. When compared to a luminosity and redshift-matched sample of *bona fide* dual AGN, AGN/no-AGN pairs exhibit one order-of-magnitude lower X-ray column density in the same separation range (>10 kpc). A small sample (4 objects) of AGN/no-AGN pairs with sub-pc separation is all heavily obscured, driving a formal anticorrelation between the X-ray column density and the galaxy pair separation in these systems. These findings suggest that the galactic environment has a key influence on the triggering of nuclear activity in merging galaxies.

Key words: galaxies: active – galaxies: interactions – galaxies: nuclei – X-rays: galaxies.

1 INTRODUCTION

The tight empirical correlations between the mass of supermassive black holes and observable quantities related to the host galaxy size (such as the M–σ relation; Ferrarese & Merritt 2000; McConnell & Ma 2013; Kormendy & Ho 2013) have been interpreted as signature of the cosmological co-evolution of accreting black holes and host galaxies. In this context, galaxy merging could play an important role in triggering the formation of black holes via direct gas collapse (Begelman, Volonteri & Rees 2006; Mayer et al. 2010), generating gas instabilities that allow the nuclear gas to lose angular momentum and efficiently feed the black hole (Di Matteo, Springel & Hernquist 2005), or even shape the environment and clustering properties of quasars (Kauffmann & Haehnelt 2000; Alexander & Hickox 2012). However, it remains unclear if there is a relation between galaxy interaction and nuclear activity. Results from X-ray and IR surveys indicate an increase of the fraction of active galactic nuclei (AGNs) in the population of merging galaxies for decreasing nuclear separation below 100 kpc (Ellison et al. 2011; Silverman et al. 2011; Satyapal et al. 2014). Also the fraction of 'dual AGNs' – close galaxy companions hosting both actively accreting black holes – increases with decreasing separation, and their X-ray luminosity increases (Koss et al. 2012). However, these conclusions are based on relatively small samples. Dual AGNs are rare, and many of the known specimen of this class have been discovered serendipitously. A robust comparison with models of galaxy mergers evolution is often cumbersome (De Rosa et al. 2019).

One of the main observational biases is the fact the AGN pairs are often heavily dust-enshrouded. It has been recently demonstrated

★ E-mail: Matteo.Guainazzi@esa.int

© 2021 The Author(s)
Published by Oxford University Press on behalf of Royal Astronomical Society

that obscured AGN show a significant excess of late-stage nuclear mergers when compared to a control sample of inactive galaxies (Koss et al. 2018). Identifying dual AGN via optical spectroscopy is therefore hard. Together with IR (Imanishi & Saito 2014), X-rays are an efficient way to detect accretion-powered processes in low-to-moderately obscured sources (i.e. Compton-thin; column density $N_{\rm H} \leq 10^{24}$ cm^{-2}), and even heavily obscured sources can be identified in deep exposures [through optically thick reprocessing spectral components; see , e.g. Piconcelli et al. (2010)], or through measurements above 10 keV (Bianchi et al. 2008; Koss et al. 2011; Iwasawa et al. 2018). Interestingly, X-ray obscuration seems also to increase with decreasing AGN separation (Ricci et al. 2017; De Rosa et al. 2018; Pfeifle et al. 2019). This is in agreement with numerical simulations (Capelo et al. 2017), even though they typically probe spatial scales ($\geq$ 50 pc) much larger than the scale of the torus where the bulk of X-ray obscuration is assumed to occur. However, these results are somewhat dependent on the sample selection criteria. Optically selected dual AGN samples tend to show a larger fraction of unobscured or moderately obscured AGN than X-ray selected samples (Green et al. 2011; Gross et al. 2019). Whether this is the correction of a bias, or a bias in itself it is still to be ascertained.

In order to increase the size of well-defined AGN pair samples, we undertook an archival project to investigate the X-ray properties of an SDSS-selected sample of galaxy pairs with separations $\leq$150 kpc containing one optically identified AGN and serendipitously observed by *XMM–Newton* (Jansen et al. 2001). The original goal of the study was identifying dual AGN pairs that may have been missed because the nuclear activity in the optical inactive galaxy remains undetected due to, for instance, heavy nuclear obscuration. The results of the study yield new observational constraints on the trigger mechanism of supermassive black holes in merging galaxies at separations $\leq$100 kpc.

The paper is structured as follows. In Section 2 we present the sample selection criteria. A reanalysis of the SDSS imaging and spectroscopy data is presented in Section 3; this is required to validate the nature of the galaxy pairs discussed in this paper. The X-ray data analysis is presented in Section 4. Our results are discussed in Section 5 and the main conclusions are summarized in Section 6.

2 SAMPLE SELECTION

In order to select the AGN/no-AGN pairs discussed in this paper, we took the SDSS DR7 galaxy sample from the MPA-JHU value added catalogues and classified all emission line galaxies into star-forming galaxies, low-ionization nuclear emission-line regions (LINERs) and Seyfert 2 galaxies using classical BPT diagnostics (Baldwin, Phillips & Terlevich 1981). All galaxies with too weak emission lines for a BPT classification (S/N<3), were assigned the class 'UNCLEAR'. Furthermore, we considered 3600 unobscured AGN from the SDSS DR7 derived catalogue of Stern et al. (2012) as Seyfert 1 galaxies. Based on the combined Seyfert 1 and Seyfert 2 catalogue we identified potential companion galaxies, classified as star forming, LINERs, or UNCLEAR, with a projected separation, R, of 5 kpc<R<200 kpc and a redshift difference of Δz<0.01. This leads to 698 Seyfert-SF pairs, 71 Seyfert-LINER pairs and 780 Seyfert-UNCLEAR pairs. We have then searched in the archive of *XMM–Newton* observations all the fields where each pair was observed at least once with at least one of the EPIC cameras. This search yielded 41 matches. 9 of these sources were later discarded because a reanalysis of the SDSS imaging and spectroscopic data did not confirm the original classification (cf. Section 3). The final list includes 32 pairs, whose coordinates and redshifts are shown in Table 1. The galaxy pairs with at least one X-ray counterpart (cf. Section 4.1) cover a range in black hole separation up to $\simeq$150 kpc, with a median separation of $\simeq$40 kpc (Fig. 1). All 32 sky positions were observed by *XMM–Newton* only once, and only a few of them were at the boresight of the corresponding observation.

Our optical selection biases the sample against heavily obscured (buried) AGN, whose ionizing photons cannot create a narrow line region (NLR). On the other hand, using X-ray spectroscopic data taken with the EPIC camera on board *XMM–Newton* for the spectral fitting may also prevent us from detecting objects whose X-ray emission is suppressed by heavy obscuration. Thus, the fraction of obscured AGN that we derive from our sample is likely to constitute a lower limit to that of the parent sample of galaxy pairs with at least one AGN. We discuss in Section 3 a way to at least partly alleviate the latter bias.

3 OPTICAL SPECTROSCOPY

Aware of possible inaccuracies in the SDSS spectroscopic classification of close galaxy pairs due to the spillover of the primary flux to the secondary fibre (Husemann et al. 2020), we retrieved the SDSS DR12 spectra (Alam et al. 2015) at the location of the galaxies, as reported in Table 1, from the survey webpage.[1] We analyse the full-band optical spectra with the software package QSFit 1.3.0 (Calderone et al. 2017), which automatically takes into account both the AGN and the host galaxy emission, together with a number of broad and narrow emission lines. In particular, we extracted the intensities of the primary diagnostic narrow emission lines such as Hβ, [O III] λ5007, [O I] λ6300, Hα, [N II] λ6583 and [S II] $\lambda\lambda$6717, 6730. Five sources (namely SSDSSJ002920.35−001028.9, SDSSJ011254.91+00031.0, SDSSJ011448.67−002946.0, SDSSJ111830.28+402554.0, and SDSSJ170601.86+601732.3) show unambiguously the presence of dominant broad components of the Balmer lines, and are therefore included in our sample. For all the other sources, the line flux ratios were then plotted in the BPT diagrams shown in Fig. 2, where the separations between Seyfert galaxies, starburst galaxies, and low-ionization nuclear emission-line regions (LINERs) are as in Kewley et al. (2006). Sources with at least one BPT diagram indicating an AGN are kept in our sample, while LINERs and all the other cases are excluded.

The ratio between the observed 2–10 keV and [O III]λ5007 luminosity in AGN is often used as a proxy of X-ray obscuration (Bassani et al. 1999), that is one of the objectives of our study. The X-ray luminosity of our sample will be discussed in the Section 4.2, while to derive the $L_{\rm [O\,III]}$ corrected for extinction, we assumed the Cardelli, Clayton & Mathis (1989) extinction law and an intrinsic Balmer decrement (Hα/Hβ) equal to 3, which represents the case for the NLR (Osterbrock & Ferland 2006). We then will use the ratio between the X-ray and [O III] λ5007 luminosity as an indirect measurement of $N_{\rm H}$ to be compared with the value obtained through X-ray spectroscopy (see Section 4.2).

4 X-RAY DATA ANALYSIS

For each of the *XMM–Newton* observations we extracted the Observation Data Files (ODFs) from the *XMM–Newton* Science Archive (XSA). The list of Observation Identifiers (Obs.#) is shown in Table 1. The data of the EPIC cameras (Strüder et al. 2001; Turner

[1] http://skyserver.sdss3.org/dr12.

Table 1. Galaxy pair sample. Column 'Minimum separation' indicates the separation (in arcmin and kpc) between the AGN and the closest galaxy in the pair. The '...' sign indicates that the values of the corresponding AGN in the system shall be applied.

Obs.#	SDSS name	RA	Dec.	z	Minimum separation	
					(')	(kpc)
04060101	SDSSJ002920.36-00102	7.33482	-0.17469	0.061	43.6	59.7
...	N/D	7.34739	-0.16365	0.060	...	...
...	N/D	7.32722	-0.18411	0.060	...	...
...	N/D	7.34890	-0.17187	0.060	...	...
0747390139	SDSSJ010951.34+00024	17.46393	0.04618	0.086	54.6	107.2
...	N/D	17.45529	0.03373	0.090	...	...
0747400142	SDSSJ011254.92+000	18.22883	0.05361	0.239	23.7	142.1
...	N/D	18.22787	0.04709	0.240	...	...
0404410201	SDSSJ011429.87+00125	18.62445	0.21521	0.046	38.6	39.4
...	N/D	18.62415	0.20448	0.050	...	...
0747400132	SDSSJ011448.68-00294	18.70279	-0.49611	0.034	8.4	6.3
...	N/D	18.70754	-0.49558	0.030	...	...
0747400150	SDSSJ011659.07+00193	19.24612	0.32593	0.078	10.1	17.9
...	N/D	19.24880	0.32673	0.080	...	...
0747430138	SDSSJ014402.61-00070	26.01089	-0.11915	0.079	55.0	98.7
...	N/D	26.02399	-0.12703	0.080	...	...
0142610101	SDSSJ030639.57+00034	46.66483	0.06197	0.107	56.5	139.9
...	N/D	46.68293	0.06610	0.110	...	...
...	N/D	46.67869	0.06935	0.110	...	...
0201120101	SDSSJ030655.63-00014	46.781	-0.02805	0.112	50.4	1.1
...	N/D	46.730	-0.01412	0.110	...	...
...	N/D	46.72687	-0.04465	0.110	...	...
0206340101	SDSSJ0852.70+16261	133.30290	16.43763	0.065	6.4	9.4
...	N/D	133.30148	16.43875	0.060	...	...
0725300159	SDSSJ090255.53+01464	135.735	1.77980	0.118	22.4	61.6
...	N/D	135.73344	1.77393	0.120	...	...
06750401	SDSSJ091507.48+29562	138.78117	29.94010	0.1	23.0	70.8
...	N/D	138.75716	29.93708	0.130	...	...
...	N/D	138.77386	29.939	0.130	...	...
0306050201	SDSSJ094046.29+03393	145.19287	3.65839	0.087	40.4	80.3
...	N/D	145.18353	3.66466	0.090	...	...
0504101701	SDSSJ101858.47+37180	154.74361	37.30021	0.048	.0	33.1
...	N/D	154.73328	37.28583	0.050	...	...
...	N/D	154.74774	37.30816	0.050	...	...
0556211401	SDSSJ104856.96+59282	162.23734	59.47383	0.093	34.9	74.4
...	N/D	162.25620	59.47245	0.090	...	...
0111290301	SDSSJ111830.29+40255	169.62616	40.467	0.155	5.5	20.4
...	N/D	169.62616	40.467	0.160	...	...
0047540601	SDSSJ114713.50+47325	176.80624	47.54950	0.074	52.5	87.9
...	N/D	176.79112	47.55992	0.070	...	...
0744040301	SDSSJ115852.20+42432	179.71750	42.72242	0.002	16.4	0.7
...	N/D	179.64188	42.73404	0.000	...	...
0601780601	SDSSJ120443.32+103	181.18051	.17729	0.025	59.7	32.6
...	N/D	181.18834	.19248	0.030	...	...
...	N/D	181.18861	.15791	0.030	...	...
...	N/D	181.18861	.15772	0.030	...	...
...	N/D	181.18834	.19248	0.030	...	...
0601780901	SDSSJ121044.28+38201	182.68446	38.33617	0.023	50.9	25.5
...	N/D	182.69930	38.34421	0.020	...	...
0722670201	SDSSJ122846.68+07275	187.19452	7.46599	0.085	8.0	15.5
...	N/D	187.19670	7.46651	0.080	...	...
0202180301	SDSSJ124210.61+370	190.54420	33.28405	0.044	55.1	53.7
...	N/D	190.52699	33.27884	0.040	...	...
0691610301	SDSSJ125729.99+28111	194.42943	27.60787	0.068	48.7	74.6
...	N/D	194.41422	27.60609	0.070	...	...
...	N/D	194.42854	27.62137	0.070	...	...
0055990501	SDSSJ133817.28+48163	204.57198	48.27563	0.028	10.1	6.2
...	N/D	204.57404	48.27807	0.030	...	...
0671150501	SDSSJ134736.41+17340	206.90169	17.56796	0.045	10.0	10.0
...	N/D	206.90462	17.56780	0.050	...	...

Table 1 – *continued*

Obs.#	SDSS name	RA	Dec.	z	Minimum separation	
					(')	(kpc)
0164560701	None	211.496	54.41608	0.083	54.6	103.2
...	N/D	211.30116	54.42896	0.080	...	...
0091140201	SDSSJ1451.76+16552	223.29903	16.92345	0.045	49.5	49.4
...	N/D	223.30621	16.93537	0.050	...	...
0721820201	SDSSJ145840.74+38273	224.66077	38.45776	0.136	25.7	82.4
...	N/D	224.66972	38.45910	0.140	...	...
0150680101	SDSSJ151811.57+172	229.54819	.28951	0.108	30.4	76.0
...	N/D	229.53943	.29341	0.110	...	...
0147210301	SDSSJ160515.86+17422	241.604	17.70761	0.0	59.7	40.6
...	N/D	241.442	17.72411	0.030	...	...
0305750301	SDSSJ170601.87+60173	256.50778	60.29233	0.130	13.5	41.2
...	N/D	256.50061	60.29357	0.130	...	...
0744410801	SDSSJ171715.74+64154	259.558	64.26115	0.035	33.5	25.8
...	N/D	259.32224	64.27000	0.030	...	...
0673000147	SDSSJ221839.93-00240	334.66635	-0.40052	0.095	30.8	67.2
...	N/D	334.67072	-0.398	0.090	...	...

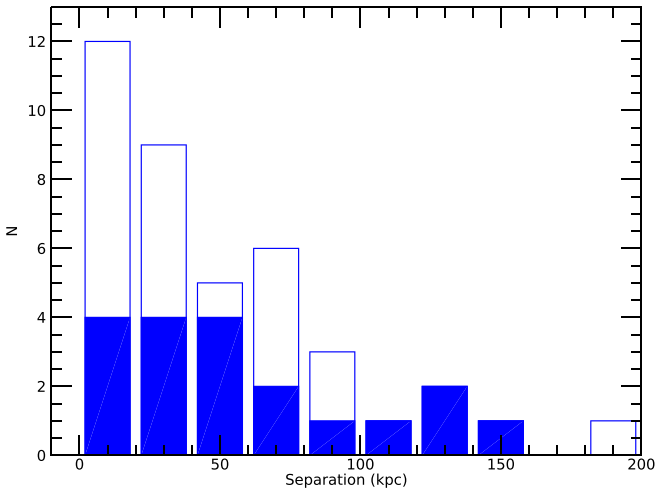

Figure 1. Histogram of the galaxy separations for the galaxies in our sample with at least one *XMM–Newton* observation (empty bars) and for those with at least one X-ray counterpart (filled bars) (cf. Table 2).

et al. 2001) were reduced using SAS version 16.0 (Gabriel et al. 2004), and the most updated calibration files available at the time the reduction was performed. Calibrated event lists were generated with the data reduction meta-tasks `epproc` and `emproc` for the EPIC-pn and the EPIC-MOS cameras, respectively. Intervals of high particle background were removed by applying a standard threshold on a representative curve of this background component, extracted using single events with energies larger than 10 keV (10–12 keV for EPIC-pn). The value of the thresholds were 0.4 and 0.35 counts s^{-1} in EPIC-pn and EPIC-MOS, respectively.

4.1 *XMM–Newton* source detection and photometry

The first step of our analysis aimed at identifying the X-ray counterparts of the sample sources. For each optically identified pair member we run the standard source detection algorithm in the SAS, through the meta-task `edetect_chain`. In a nutshell, this task employs the detection algorithm in Cruddace, Hasinger & Schmitt (1988) on an image whose background is determined through a 2-D spline of field-of-view map from which sources had been removed on the basis of a prior detection run. We run the detection algorithm simultaneously on EPIC-pn and EPIC-MOS images in the 0.3–10 keV energy band extracted on a square box of 2 arcmin size around the nominal coordinates of the optically identified AGN. We used a `edetect_chain` option allowing to simultaneously fitting the telescope Point Spread Function (PSF) in the so-called 'multisource mode' (with input parameters `nmulsou` = 2 and `scut` = 200), where neighbouring sources with overlapping PSFs are fitted simultaneously. Our choice is driven by the fact that the distance between the components of some of the pairs in our sample is comparable with the telescope angular resolution. Following Rosen et al. (2016), we assume that an X-ray source is a *bona fide* counterpart of an optical galaxy if the centroid distance is $\leq$3.5".

We show the results of our X-ray photometric analysis in Table 2. For each optically identified AGN we list one row for each of the potentially associated AGN/non-AGN pair members. We significantly detect 19 X-ray sources among the optically identified AGN. For completeness, in the other cases we show the distance of the closest X-ray source in the 2 arcmin side detection box, if any.

Among the galaxies optically classified as 'non-AGN', only one X-ray source is detected within the aforementioned astrometric error: a galaxy with coordinates (RA,Dec.) = (133.30148,16.43875), companion to the AGN SDSS J0852.70+16261 in Obs.#0206340101. Its total 0.3–10 keV count rate is $(9 \pm 3) \times 10^{-3}$ s^{-1}. It belongs to the galaxy pair in our sample corresponding to the smallest separation (6.4 arcsec), comparable to the angular resolution of the X-ray telescope. This casts doubts on the robustness of the detection that could be affected by uncertainties in the Point Spread Function modelling (Fig. 3). For all the other non-AGN galaxies, upper limits on an X-ray counterpart vary in the range between 0.011 and 5 s^{-1} depending on the source position in the EPIC field of view and the observation exposure time.

4.2 *XMM–Newton* spectroscopy

For each of the X-ray counterparts, we performed a formal forward-folding spectral analysis. Our main goal is to estimate the X-ray luminosity and the column density obscuring the primary emission of the AGN. EPIC source spectra were extracted from a circular region of 20 arcsec radius around the SDSS optical position. Background

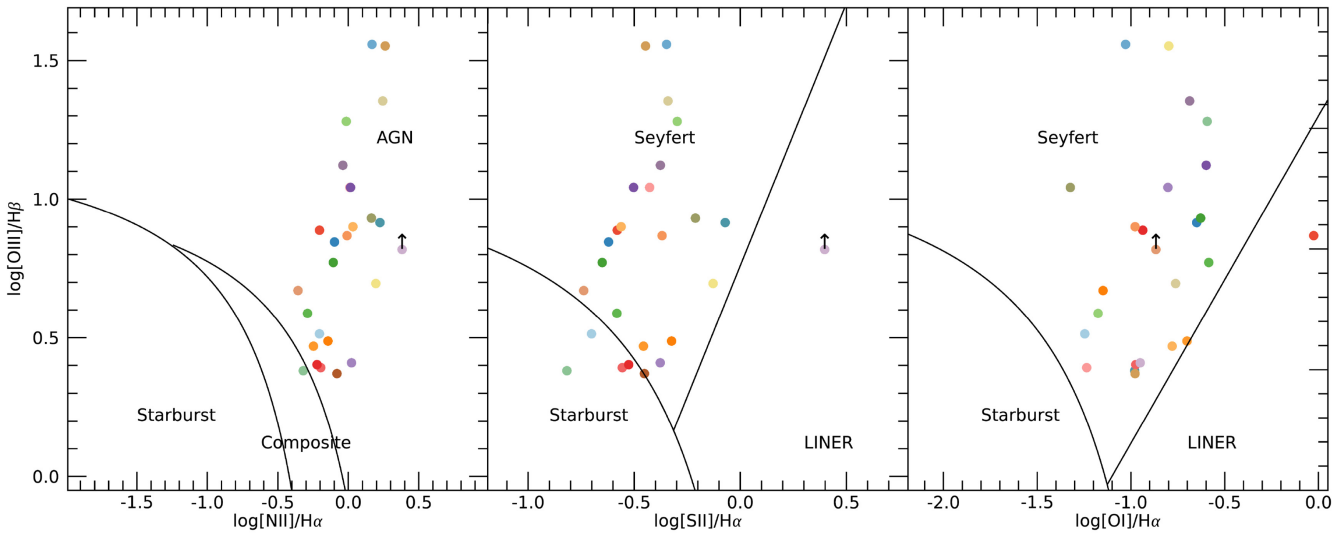

Figure 2. BPT diagrams for all the sources of our sample. See the text for details.

spectra were extracted from boxes in detector coordinates of 50 arcsec × 75 arcsec and 50 arcsec × 150 arcsec once a circle around the AGN had been removed with a radius comprised between 30 and 40 arcsec depending on the source count rate to avoid that the background region is contaminated by the source PSF wings. From the background regions circles were also excised around any serendipitous source (including the position of the non-active SDSS AGN). Instrument responses were generated for each individual source using the standard SAS tasks `rmfgen` and `arfgen` taking into account the corresponding time- and spatial-dependent calibration.

Spectra were rebinned according to the instrumental resolution following the prescription in Kaastra & Bleeker (2016). Spectra were analysed in the 0.3–10 keV energy range using the Cash statistics (Cash 1976; Kaastra 2017). We have employed a set of phenomenological models as described in Table 3.[2] They are sufficient to describe the spectral shapes observed in the X-ray spectra of the AGN on our sample. While a detailed physical description of the astrophysical nature of each object is beyond the scope of this paper, the proposed parametrization is sufficient to allow us to estimate the quantities we are interested in (X-ray luminosity and obscuring column density), keeping the systematic uncertainties due to the models lower than the statistical errors. As far as the Compton-reflection model is concerned ($R(E)$ in Table 3), we used `pexrav` (Magdziarz & Zdziarski 1995) for consistency with the results published in the literature on sources of similar statistical quality and for simplicity, even if we are well aware of the existence of more recent and sophisticated models to describe the emission from the AGN torus (see, e.g. the discussion in Murphy & Yaqoob 2009). As we are not interested in this paper in understanding the detailed properties of the reprocessing material (that would be anyway very hard to determine given the quality of the spectroscopic data) we consider this approximation acceptable. In using `pexrav` we have assumed that the spectral index of the primary illuminating continuum is the same as that of the primary continuum, and that the cut-off energy is 100 keV. This value is consistent with the measurement in several nearby AGN observed with NuSTAR (Tortosa et al. 2018; Middei et al. 2019). the exact value of this parameter does not have an impact on the results discussed in this paper. Likewise, we employed models of optically thin, collisionally ionized plasma (`apec`; Smith et al. 2001) to model any 'soft excess' component above the extrapolation of the hard X-ray power law (assumed of nuclear origin) not to unduly overfit the spectroscopic data, even if there is now overwhelming evidence that any 'soft excess' in obscured AGN is due to the emission of photoionized gas in the X-ray Extended NLR (Kinkhabwala et al. 2002; Guainazzi & Bianchi 2007; Bianchi et al. 2019), while the origin of the soft excess in unobscured AGN is still debated (Crummy et al. 2006; Fabian et al. 2009; Done et al. 2012). None of these assumptions affects substantially the main conclusions of this *paper*.

As the Cash goodness-of-fit test does not allow us to estimate the absolute quality of the fit, the best-fitting model was chosen by applying an empirical criterion to models differing by one component corresponding to the 99 per cent confidence level of the *F*-test calculated on the basis of the χ^2 difference between the two models, taking the caveats after Protassov et al. (2002) into account. We applied the χ^2 on spectra rebinned to a minimum number of 10 counts per background-subtracted spectral channel to minimize biases due to the non-Gaussian nature of the count distribution.

The quality of the X-ray spectroscopic data is insufficient to constrain the primary photon index when: a) the hard X-ray spectrum is dominated by a Compton-reflection component (Model #5 in Table 3); b) in a few sources where the primary continuum is heavily obscured and therefore the number of counts above the photoelectric cut-off energy is too low. In these cases we have assumed a photon index fixed to the value $\Gamma = 1.7$, the median value observed in a sample of nearby AGN with good quality X-ray spectroscopy data with *XMM–Newton* (Bianchi et al. 2008). In two objects (SDSS J002920.36-00102 and SDSS J011254.92+00) the AGN photon index can be measured, but is marginally inconsistent with this value because it is too hard. We attribute this discrepancy to poor signal to noise (in the latter case in presence of a steeper soft X-ray component). We estimate that the corresponding systematic error on the AGN X-ray luminosity is $\leq$20 per cent if $\Gamma = 1.7$ is the true value. In SDSS J120443.32+103 a flat spectral index $\Gamma \simeq 1.2$ is measured in a good signal-to-noise spectrum. In this case, we

[2]In the analysis we used a wider set of trial models than shown in Table 3, which include only those yielding the best-fit on at least one of the sources in Table 4.

Table 2. Total 0.3–10 keV count rate of the X-ray counterparts of the *bona fide* optically identified AGNs in our sample, as estimated from the combined EPIC images of the corresponding *XMM–Newton* observation. Rows in bold indicate AGN with an identified *bona fide* X-ray counterpart. An upper limit at the optical position (1σ-level) is shown if the closest X-ray source is located at a distance larger than the astrometric error of the *XMM–Newton* EPIC serendipitous source catalogue (3.5 arcsec at the 90 per cent confidence level). The 'Distance' is between the AGN optical position and the closest X-ray source in the 2 arcmin × 2 arcmin detection box. The dots indicate AGN optical positions for which no meaningful X-ray count rate upper limit could be estimated and/or no X-ray source was detected in the detection box.

Source ID	Rate (s^{-1})	Net counts	Distance (')
SDSSJ002920.36-00102	**0.688 ± 0.040**	**2533 ± 125**	**0.1 ± 2.9**
SDSSJ010951.34+00024	**0.115 ± 0.017**	**222±24**	**5.8 ± 4.3**
SDSSJ011254.92+000	**0.630 ± 0.017**	**1477 ± 40**	**0.7 ± 0.2**
SDSSJ011429.87+00125	≤0.023	6632 ± 199	12.8 ± 1.2
SDSSJ011448.68-00294	...	...	...
SDSSJ011659.07+00193	**0.152 ± 0.014**	**326 ± 28**	**6.1 ± 3.4**
SDSSJ014402.61-00070	**0.042 ± 0.005**	**110 ± 12**	**1.1 ± 1.0**
SDSSJ030639.57+00034	**0.948 ± 0.005**	**33992 ± 189**	**0.9 ± 0.0**
SDSSJ030655.63-00014	**0.729 ± 0.046**	**4564 ± 286**	**2.9 ± 2.8**
SDSSJ0852.70+16261	**0.223 ± 0.008**	**2332 ± 73**	**1.3 ± 0.8**
SDSSJ090255.53+01464	≤0.039	13 ± 5	77.4 ± 7.2
SDSSJ091507.48+29562	≤0.022	1604 ± 100	19.6 ± 2.7
SDSSJ094046.29+03393	≤0.019	2097 ± 93	56.5 ± 0.8
SDSSJ101858.47+37180	**0.522 ± 0.023**	**2379 ± 103**	**0.6 ± 0.9**
SDSSJ104856.96+59282	**0.289 ± 0.009**	**1129 ± 36**	**1.4 ± 0.3**
SDSSJ111830.29+40255	≤2.553	6046 ± 343	56.3 ± 0.0
SDSSJ114713.50+47325	≤0.014	762 ± 259	69.0 ± 1.4
SDSSJ115852.20+42432	**0.1 ± 0.005**	**1249 ± 43**	**2.1 ± 0.7**
SDSSJ120443.32+103	**0.648 ± 0.006**	**15460 ± 129**	**0.5 ± 0.1**
SDSSJ121044.28+38201	**0.601 ± 0.040**	**1858 ± 47**	**1.3 ± 0.2**
SDSSJ122846.68+07275	...	...	...
SDSSJ124210.61+370	**7.121 ± 0.028**	**66480 ± 258**	**0.6 ± 0.0**
SDSSJ125729.99+28111	**0.433 ± 0.011**	**5324 ± 126**	**3.6 ± 1.1**
SDSSJ133817.28+48163	≤0.266	3911 ± 270	19.6 ± 0.2
SDSSJ134736.41+17340	**0.145 ± 0.005**	**887 ± 33**	**1.6 ± 0.3**
SDSSJ1451.76+16552	≤0.022	3237 ± 262	9.0 ± 1.3
SDSSJ145840.74+38273	**0.356 ± 0.015**	**3681 ± 155**	**3.5 ± 2.6**
SDSSJ151811.57+172	≤0.021	3652 ± 170	71.6 ± 1.7
SDSSJ160515.86+17422	0.711 ± 0.026	4360 ± 146	5.2 ± 0.7
SDSSJ170601.87+60173	**0.241 ± 0.056**	**48 ± 7**	**1.4 ± 1.2**
SDSSJ171715.74+64154	**0.004 ± 0.002**	**52 ± 13**	**4.0 ± 0.7**
SDSSJ221839.93-00240	≤0.025	≤ 41	8.5 ± 1.4

Table 3. List of models used in the spectroscopic analysis of the AGN counterpart. A is the power-law normalization. $G(E)$ is a Gaussian profile in emission. $C(E)$ describes the emission of an optically thin, collisionally ionized plasma in thermal equilibrium (Smith et al. 2001). $R(E)$ is a Compton-reflection model after Magdziarz & Zdziarski (1995).

ID	Model
1	$e^{-\sigma N_H} A_1 E^{-\Gamma}$
2	$A_1 E^{-\Gamma} + e^{-\sigma N_H} A_2 E^{-\Gamma}$
3	$A_1 E^{-\Gamma} + e^{-\sigma N_H} A_2 E^{-\Gamma} + G(E)$
4	$C(E) + e^{-\sigma N_H} A E^{-\Gamma}$
5	$C(E) + R(E) + G(E)$

interpret this results as due to a too simple parametrization of the X-ray absorber as a single layer. While more complex X-ray absorption structures are not required by the fit, it is possible that deep X-ray observations at higher energies may unveil an additional, higher column density component. If this is the case, our measurement of the column density in this object, $\simeq 6 \times 10^{22}$ cm^{-2}, is likely to represent a lower limit to the true column density covering the AGN.

The best-fitting values on 2-10 keV observed luminosity, photon index, and column density absorbing the primary continuum are shown in Table 4. We have complemented the results of the X-ray spectral analysis through a study of the ratio between the observed 2–10 keV and [OIII]λ5007 luminosities. This is known to be a sensitive diagnostic of X-ray obscuration (Bassani et al. 1999; cf. Section 3 for the derivation of the [O III] luminosity). The selection criteria of our sample, extracted from optically classified AGN/no-AGN pairs (cf. Section 2), ensure that we can use it as a proxy for X-ray obscuration. The $L_x/L_{[O\,III]}$ ratio has been investigated using different samples of type 1 and type 2 AGNs (Mulchaey et al. 1994; Bassani et al. 1999; Heckman et al. 2005; Lamastra et al. 2009; Vignali et al. 2010). In particular, in a sample of Compton-thick AGN Marinucci et al. (2012) measured log $(L_x/L_{[O\,III]}) = -0.76$ (0.1 dex dispersion), while for Compton-thin AGN Lamastra et al. (2009) found log $(L_x/L_{[O\,III]}) = 1.09$ (0.63 dex dispersion). We will use these thresholds to shed further light on the source classification based on the X-ray spectral analysis. We assumed a threshold of log $(L_x/L_{[O\,III]}) \leq 0.43$ to classify a source as Compton-thick. Out of the *bona fide* AGN of our sample, eight sources have a ratio value indicative of Compton-thick obscuration. For these sources we estimate a 2–10 intrinsic luminosity larger than the observed one by a factor of 70, following Lamastra et al. (2009), Marinucci et al. (2012). We have also verified *a posteriori* that all sources with a log $(L_x/L_{[O\,III]})$ between 0.43 and 1.72 are consistent with being Compton-thin according to the X-ray spectral analysis, except one for which only a log $(N_H) \leq 21.82$ upper limit on the X-ray column density (for a rather steep photon index: $\Gamma \geq 2.4$) could be determined.

We did not perform any spectral analysis on the only X-ray counterpart of the SDSS non-active member of the pairs due to the low statistical quality of the detection (cf. Section 4.1). Its count rate corresponds to an observed flux of $(6 \pm 2) \times 10^{-14}$ erg s^{-1} cm^{-2}, or an observed rest-frame luminosity of $(5.3 \pm 1.8) \times 10^{41}$ erg s^{-1}, for a typical unobscured ($N_H = 5 \times 10^{20}$ cm^{-2}) AGN power-law spectrum with a $\Gamma = 2$ photon index.

4.3 Radio emission

We correlated the position of the AGN in the parent sample of 32 galaxy pairs with the Faint Images of the Radio Sky at Twenty-Centimers (FIRST; Helfand, White & Becker 2015) and the NRAO VLA Sky Survey (NVSS; Condon et al. 1998) 1.4 GHz radio surveys, using a matching radius of ≤3.5" driven by the X-ray astrometric accuracy. 12 of the X-ray sources exhibit a radio counterpart. A radio source is present at the position of 5 additional AGN with no detected X-ray counterpart. About half of the AGN are X-ray overluminous with respect to the radio luminosity when compared to the relation derived from a sample of local Seyfert 1 galaxies [$L_X = (11.60 \pm 0.72) + (0.81 \pm 0.02) \times L_R$] (Fig. 4; Panessa et al. 2007).

Table 4. Best-fitting parameters for the X-ray counterparts of the optically classified AGNs. N_H is the column density covering the primary continuum; L_X is the 2–10 keV luminosity of the primary continuum corrected for absorption; Γ is the photon index of the primary power-law continuum; log ([O III]) is the [O III]λ5007 luminosity; BD is the Balmer Decrement; log (R) is the logarithm of the ratio between the observed 2–10 keV and BD-corrected [O III] luminosity (cf. Section 3). N/A indicates that the [O III] measurement is not available. The Model IDs follow Table 3.

Source	log (L_X)	log (N_H)	Γ	log ($L_{[O\,III]}$)	log (BD)	log (R)	Model	C/ν
SDSSJ002920.36-00102	$42.29\pm^{0.38}_{0.17}$	$22.91\pm^{0.88}_{1.16}$	$0.57\pm^{1.07}_{1.34}$	39.67	−0.7	2.6	3	103.9/87
SDSSJ010951.34+00024	$43.55\pm^{0.33}_{0.50}$	≥24.20	$1.7^{\dagger}$	41.77	0.7	−0.1	5	11.5/15
SDSSJ011254.92+000	$43.49\pm^{0.13}_{0.28}$	≤24.25	$0.28\pm^{1.37}_{0.87}$	39.45	−2.2	4.0	2	190.2/217
SDSSJ011659.07+00193	$43.23\pm^{0.53}_{0.67}$	≥24.20	$1.7^{\dagger}$	41.65	1.6	−0.3	1	38.8/25
SDSSJ014402.61-00070	≤43.35	≥24.20	$1.7^{\dagger}$	41.56	1.4	≤-0.2	5	56.1/44
SDSSJ030639.57+00034	$42.77\pm^{0.92}_{0.18}$	$21.55\pm^{0.25}_{0.74}$	$1.84\pm^{0.05}_{0.04}$	41.34	−0.2	1.4	2	543.8/494
SDSSJ030655.63-00014	$44.31\pm^{0.25}_{0.24}$	≥24.20	$1.7^{\dagger}$	42.24	1.4	0.2	5	96.7/97
SDSSJ0852.70+16261	$42.58\pm^{0.10}_{0.08}$	$23.00\pm^{0.18}_{0.20}$	$1.48\pm^{0.64}_{0.55}$	41.05	0.4	1.5	2	284.0/277
SDSSJ101858.47+37180	$43.09\pm^{0.23}_{0.24}$	≥24.20	$1.7^{\dagger}$	41.43	0.6	−0.2	1	95.6/90
SDSSJ104856.96+59282	$42.85\pm^{0.07}_{0.07}$	$-0.15\pm^{0.19}_{0.}$	$1.61\pm^{0.18}_{0.17}$	40.91	0.1	1.9	1	263.5/247
SDSSJ115852.20+42432	$40.66\pm^{0.14}_{0.14}$	≥24.20	$1.7^{\dagger}$	39.24	1.2	−0.4	4	439.4/149
SDSSJ120443.32+103	$42.61\pm^{0.01}_{0.02}$	$22.76\pm^{0.04}_{0.05}$	$1.23\pm^{0.09}_{0.11}$	41.57	0.4	1.0	3	653.4/523
SDSSJ121044.28+38201	$42.55\pm^{0.45}_{0.37}$	$23.17\pm^{0.13}_{0.13}$	$1.48\pm^{0.67}_{0.72}$	39.80	−1.0	2.7	2	277.5/304
SDSSJ124210.61+370	$43.20\pm^{0.02}_{0.02}$	$22.06\pm^{0.08}_{0.06}$	$1.79\pm^{0.08}_{0.06}$	41.45	0.0	1.8	3	802.6/498
SDSSJ125729.99+28111	$-0.31\pm^{0.10}_{0.}$	$22.48\pm^{0.14}_{0.13}$	$1.48\pm^{1.26}_{0.84}$	N/A	N/A	N/A	2	197.6/185
SDSSJ134736.41+17340	$41.73\pm^{0.24}_{0.34}$	≥24.20	$1.7^{\dagger}$	41.44	0.5	−1.6	1	195.6/167
SDSSJ145840.74+38273	$42.21\pm^{0.36}_{0.52}$	≥24.20	$1.7^{\dagger}$	N/A	N/A	N/A	5	214.6/199
SDSSJ170601.87+60173	$42.27\pm^{0.69}_{0.71}$	≤21.82	$3.53\pm^{1.99}_{1.09}$	41.08	0.2	1.2	1	16.9/22
SDSSJ171715.74+64154	$41.97\pm^{0.65}_{1.40}$	≥24.20	$1.7^{\dagger}$	41.90	1.8	−1.8	1	93.0/64

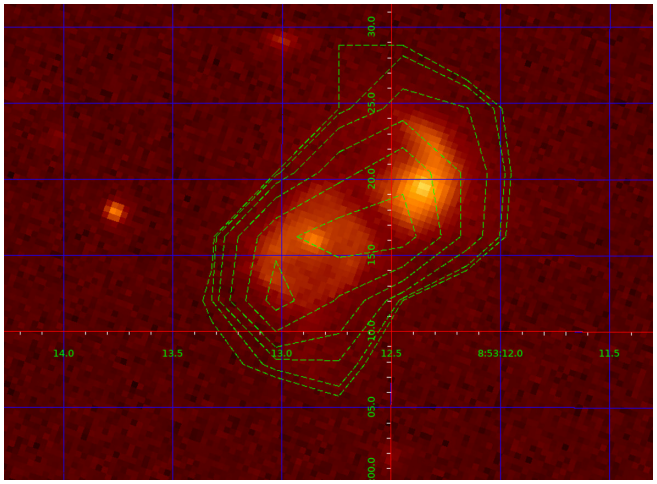

Figure 3. SDSS i-filter image superposed to the count contours of the EPIC image (green dashed lines; six levels in logarithmic scale in the 10–42 net EPIC counts per pixel range) for the only galaxy pair where an X-ray counterpart spatially coincident with each member of the pair is detected: SDSS J0852.70+16261.

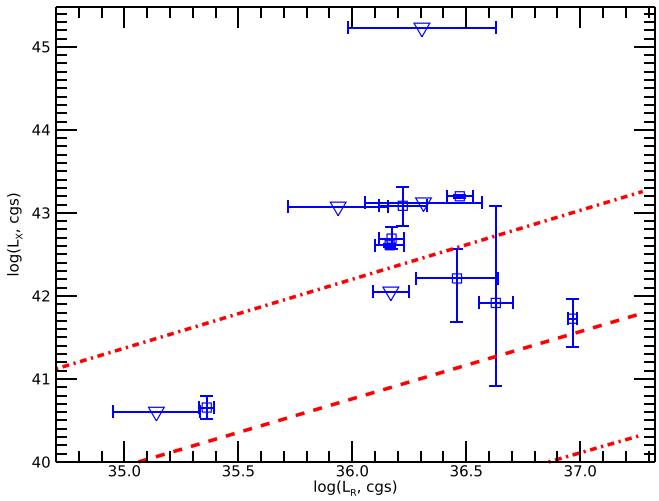

Figure 4. X-ray (L_x) versus 1.4 GHz luminosity (L_R) for the AGNs in the galaxy pair sample discussed in the paper. Downward triangles indicate upper limits on the X-ray luminosity. The red lines represent the best-fitting linear relation (dashed) and the envelope corresponding to the 1σ uncertainty on the best-fitting parameters (dot–dashed) of the relation between the 2–10 keV luminosity and the 20 cm radio luminosity on the sample of local Seyfert galaxies after Panessa et al. (2007).

5 DISCUSSION

5.1 The X-ray counterparts of inactive galaxies

Only 1 out of 32 galaxies optically classified as non-AGN is our sample has a *bona fide* X-ray counterpart. It is the companion galaxy of the AGN SDSS J0852.70+16261. The detection is at the 3σ level only (110 ± 40 total net counts) preventing a detailed spectral analysis. Moreover, it corresponds to the galaxy pair with the smallest separation in our sample (6.4 arcsec), comparable to the angular resolution of the X-ray telescope. Assuming it is a *bona fide* detection, and a standard unobscured AGN spectrum, its observed rest-frame luminosity ($\simeq 5 \times 10^{41}$ erg s^{-1}) is consistent with a weak AGN, a heavily obscured Seyfert galaxy, emission from starbursts (although in this case it would correspond to a rather extreme Far Infrared Luminosity of $\sim 10^{45}$ erg s^{-1} for the local Universe; Ranalli, Comastri & Setti 2003), or even an extreme ultra-luminous X-ray (ULX) source. Its *Florence and George Wise Observatory* (WISE) colours (Table 5) correspond to an intermediate region where obscured AGN may be located (Ricci et al. 2017; Weston et al. 2017). They are close to the WISE colours of the pair of X-ray obscured AGN ESO509-IG066 (Guainazzi et al. 2005). An obscured AGN is also suggested by the *Chandra* spectrum (Hou et al. 2020).

Table 5. WISE colours for SDSS J0852.70+16261 and its companion galaxy.

WISE name	W1–W2	W2–W3
J0852.38+162619.7	0.355	4.064
J0852.87+162615.7	0.845	3.145

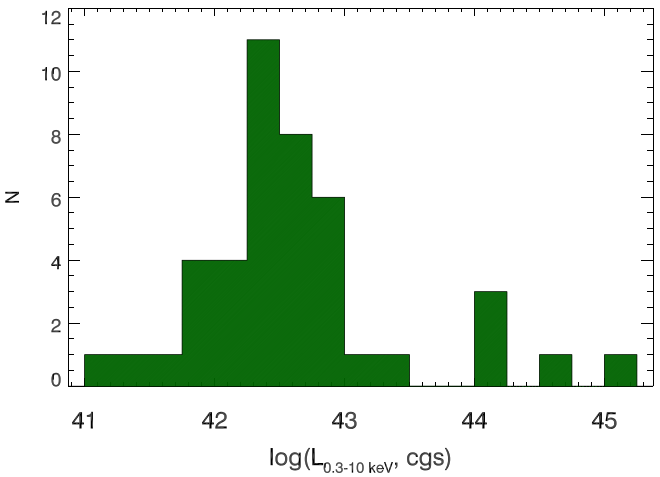

Figure 5. 90 per cent confidence level upper limits on the 0.3–10 keV observed rest-frame luminosity at the position of the galaxies optically classified as 'non-AGN' is our sample.

The nature of the X-ray emission in galaxies without detected X-ray counterparts remains elusive. In Fig. 5, we show the upper limits on the 0.3–10 keV observed rest-frame luminosity at the position of the galaxy optical centroid. In all cases, the upper limits exceed 10^{41} erg s^{-1}, and 10^{42} erg s^{-1} for >90 per cent of the sample. Deeper observations would be needed to either detect AGN still confused in the observation noise, or to rule out with certainty the presence of weak of heavily obscured AGN in these optically inactive galaxies. Further observations with *Chandra* would also surely help in ensuring that weak sources are not confused by the comparatively large and complex PSF of the *XMM–Newton* telescope.

5.2 AGN triggering in AGN/no-AGN galaxy pairs

In order to make a statistical analysis of the obscuration in merging galaxies, we collected from literature the systems hosting AGN/no-AGN pairs and for which a measure of the absorption column density can be derived from X-ray observations. We selected from literature additional 14 pairs AGN-galaxy in different wavebands (Ricci et al. 2017; Satyapal et al. 2017; Hou et al. 2019; Pfeifle et al. 2019). Together with our systems with measured value of N_H, we collected a total sample of 33 systems (see Tables 4 and 6). We compared this enlarged sample with both a sample of dual AGN (the ≃60 objects extracted from an heterogeneous literature sample by De Rosa et al. (2018); see also Ricci et al. (2017)) and with a sample of isolated AGN (728 non-blazar AGNs extracted from the 70-month catalogue of the *Swift*/BAT; Ricci et al. (2015)) in the same range of X-ray luminosities (5×10^{40}–2×10^{44} erg s^{-1}).

In Fig. 6, we show the evolution of the X-ray column density as a function of galaxy separation. The data points represent the AGN/no-AGN sample. Given the large number of censored data, we fit the data with a Monte Carlo method, whereby 10 000 sets of simulated data sets were drawn from the observed data set by:

Table 6. Separations, s, and column densities, N_H, for the additional AGN/no-AGN systems extracted from the literature.

Source	s (kpc)	log (N_H)
IRAS05189-2524	0.1	$23.10\pm^{0.03}_{0.04}$
Mrk2	0.1	$23.16\pm^{0.08}_{0.10}$
NGC 34	0.1	$23.72\pm^{0.08}_{0.10}$
UGC05101	0.1	$24.12\pm^{0.09}_{0.12}$
NGC 7130	0.1	$24.30\pm^{0.18}_{0.30}$
IRAS120-5453	0.1	$24.50\pm^{0.24}_{0.23}$
J1036+0221	2.8	$21.85\pm^{0.06}_{0.07}$
J2356-1016	5.0	$22.93\pm^{0.08}_{0.10}$
J1147+0945	6.8	$22.41\pm^{0.05}_{0.05}$
J0859+10	9.9	$23.24\pm^{0.11}_{0.12}$
NGC 4922N	10.8	≥24.20
CG468-002W	11.3	$22.18\pm^{0.03}_{0.03}$
NGC 7674	20.7	≥24.20
NGC 7469	26.0	$19.78\pm^{0.12}_{0.18}$

a) replacing each column density constrained measurement with the sum of the best-fitting value and the statistical error multiplied by a random number extracted from a Gaussian distribution of mean zero and unitary standard deviation; b) replacing each column density censored measurement with a value randomly extracted from a uniform distribution in the [LL,10^{19} cm^{-2}] and [UL, 10^{26} cm^{-2}] for lower limits (LL) and upper limits (UL), respectively. The curves in Fig. 6 represent the average of the fit on the 10 000 simulated data sets (dotted) and the 1σ envelope (dashed–dotted of the best-fitting curves distribution. Formally, a strong anti-correlation between X-ray obscuration and galaxy separation is found, with average N_H decreasing from a few 10^{23} to ∼10^{22} cm^{-2} from the subkpc to the ∼100 kpc scale. However, a few caveats shall be borne in mind. The correlation is driven by a few heavily obscured sources at subkpc scale. If they are removed from the fit, the anti-correlation between X-ray obscuration and galaxy separation in the AGN/no-AGN systems becomes statistically not significant. Furthermore, at separations larger than 10 kpc a sizeable number of Compton-thick objects are found. However, the formal anti-correlation is only marginally affected by the inclusion/removal of the Compton-thick sources (due to their homogeneous distribution along the separation axis).

Out of the 19 sources in our sample for which measurements of the Balmer Decrement (BD) and of the X-ray obscuration are available, 7 out of 9 objects with BD ≥ 2, and all the 7 objects with BD ≥ 3 are X-ray Compton-thick. For lower values of the Balmer Decrement no correlation with the X-ray column density is found. This may indicate that the highest obscuration in the NLR of these systems is associated with the most compact structures surrounding the active nuclei, possibly the torus. No constraints on the location of the Compton-thin obscurer can be derived from the data our sample. It is well possible that Compton-thick and -thin absorbers in the AGN our sample probe entirely different systems, thus complicating the interpretation of the correlation shown in Fig. 6.

With this caveat in mind, the red curve in Fig. 6 represents the results of the same fit procedure applied to the dual AGN sample. In the common separation range (≥10 kpc), dual AGN exhibit an

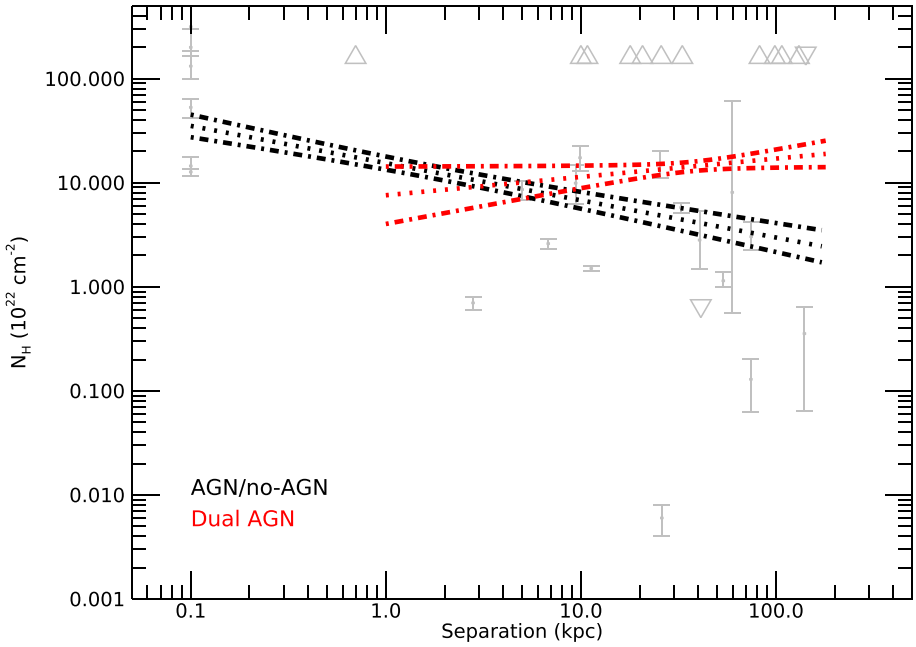

Figure 6. X-ray nuclear column density versus galaxy separation for the AGN/no-AGN sample. The light silver data points represent the measurements presented in this paper augmented of the literature systems listed in Table 6. Upward (downward) triangles represent lower (upper) limits. The black lines represent the best-fit (dotted) and the envelope corresponding to the 1σ statistical uncertainties (see details of the fit procedure in the text). The red lines represent the same fit for a sample of *bona fide* dual AGN (data not shown).

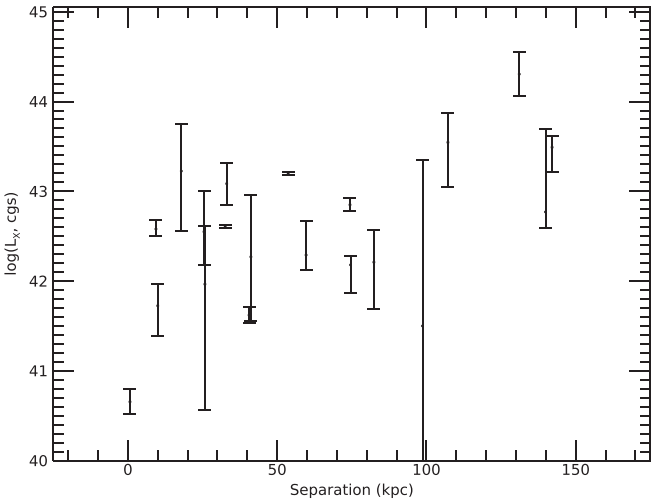

Figure 7. X-ray nuclear luminosity (in logarithm of cgs units) as a function of galaxy pair separation in the AGN/no-AGN sample presented in this paper.

X-ray obscuration higher by above one order of magnitude than the AGN/no-AGN pairs. The lack of dual AGN corresponding to sub-kpc galaxy separation prevents us from extending this comparison to the most compact systems. The total fraction of 'obscured' AGN ($N_{\rm H} \geq 10^{22}$ cm^{-2}) in the AGN/no-AGN sample is comprised between 79 per cent and 84 per cent (cf. Table 4). This is significantly larger than observed in isolated AGN of comparable nuclear luminosity ($\simeq$45 per cent; Ricci et al. 2015). It is, however, comparable to the fraction of obscured AGN in a dual AGN sample that raises slowly from $\simeq$70 per cent at galaxy pair separations larger than 60 kpc to almost 90 per cent for separations lower than 20 kpc.

In Fig. 7, we show the nuclear X-ray luminosity as a function of galaxy separation for the *bona fine* AGN presented in this *paper*. A linear fit with a function: $\log(L_{\rm X}) = A + B \times s$ (where s is the galaxy pair separation in kpc) yields a moderate trend for more compact systems to be less luminous: $A = 42.05 \pm 0.03$, and $B = 0.0178 \pm 0.0008$ kpc^{-1}, corresponding to a decrease of 1 dex in luminosity per $\sim$60 kpc. However, it should be borne in mind that our sample is neither complete nor unbiased in any sense. It is therefore hard to assess the significance of such a weak trend on the unknown parent population.

Both cosmological (Steinborn et al. 2016; Volonteri et al. 2016) and idealized hydrodynamic simulations (Blecha et al. 2016; Capelo et al. 2017) of merging galaxies hosting BH have been extensively investigated in order to evaluate the main parameters triggering the AGN activity in interacting galaxies. In particular, numerical simulations show an increase of $N_{\rm H}$ as the distance decreases, due to merger dynamics. The simulation predict a median value of $N_{\rm H}$ of $\sim 3 \times 10^{23}$cm^{-2}, that is in good agreement with the value measured in sample of dual AGN (De Rosa et al. 2018). It worth noticing that the spatial resolution of the simulation only allow to probe absorption on relatively large scales (above $\sim$ 50 pc), this means that absorption from the AGN torus, on typical pc-scale, is not considered and then the $N_{\rm H}$ value from simulations represents a lower limit.

Simulations of the dynamical evolution of isolated mergers indicate that the evolution depends in principle on several parameters of these complex systems: galaxy morphology, bulge-to-disc stellar mass ratio, orbital configuration, galaxy mass ratio, bulge-to-disc mass ratio, galaxy mass ratio, black hole mass ratio, and the black hole feedback efficiency (Van Wassenhove et al. 2012; Blecha et al. 2016, 2018; Capelo et al. 2017). All simulations in general agree on the dual AGN phase to be short, primarily concentrated when the two black holes are separated by less than $\sim$10 kpc. For typical AGN luminosities $\geq 10^{42}$ erg s^{-1}, pairs of merging galaxies are supposed to spend just a few Myr in a 'dual AGN' phase (Capelo et al. 2015). At black hole separations $\geq$10 kpc, the fraction of the dual active phase versus the total active phase (i.e. the phase when at least

one of the AGNs is actively accreting) goes from a few per cent to about 20 per cent. As our sample was pre-selected as galaxy pairs constituted by an active and an inactive galaxy (according to an optical spectroscopic classification), it does not allow a direct comparison with the predictions of merging simulations. However, when this comparison is possible (e.g. against the all-sky *Swift*-BAT survey; Koss et al. 2012) consistency between the fraction of dual AGNs in a galaxy sample and the simulation predictions within a factor of two was found.

6 CONCLUSIONS

In this paper, we present an *XMM–Newton* study of a sample of galaxy pairs, identified through SDSS spectroscopy as being constituted by an AGN-hosting and an inactive galaxy. The original main goal of the project was to identify via X-rays active nuclei in the 'inactive' member of the pair that could have been missed due to heavy obscuration along the line of sight to the nucleus. For the galaxies hosting an AGN, we discuss in this paper the X-ray photometric and spectroscopic properties, and put them in context of the prediction of state-of-the-art hydrodynamical simulations of isolated mergers on the condition for the triggering of 'dual' AGN.

Out of the parent sample of over 1500 galaxy pairs with an SDSS 'AGN–no-AGN' classification, 32 *bona fide* pairs are in the field of view of the EPIC cameras (as of March 2018). The main results of our study can be summarized as follows:

(i) for only one of the 'non-AGN' galaxies in the pair an X-ray counterpart is found (at the 3σ level). Assuming a standard AGN-like X-ray spectrum, its rest-frame luminosity ($\simeq 5 \times 10^{41}$ erg s^{-1}) is consistent with a weak AGN, a heavily obscured Seyfert galaxy (consistently with its WISE colours), emission from starbursts, or even an extreme ULX source;

(ii) for 90 per cent of the 'non-AGN galaxies' in the pair for which no X-ray counterpart is found, the derived upper limits on the 2-10 keV luminosities are $\geq 10^{42}$ erg s^{-1}, i.e. still consistent with an active nucleus 'hidden' in the data (cf. Fig. 5);

(iii) for 19 'AGN' galaxies in the pair, a *bona fide* X-ray counterpart is found, covering a wide range in absorption corrected X-ray luminosity (5×10^{40}–2×10^{44} erg s^{-1}; cf. Table 4);

(iv) our AGN/no-AGN sample shows only a weak dependence of the AGN X-ray luminosity on the separation between the members of the galaxy pair, with more compact systems being marginally *less luminous* (cf. Fig. 7);

(v) the *bona fide* AGNsare unevenly split between 'unobscured' ($N_{\rm H} < 10^{22}$ cm^{-2}; 16–26 per cent), 'Compton-thin ($10^{22} \leq N_{\rm H} < 1.6 \times 10^{24}$ cm^{-2}; 32–37 per cent), and 'Compton-thick' ($N_{\rm H} \geq 1.6 \times 10^{24}$ cm^{-2}; 47 per cent) obscured (cf. Table 4);

(vi) we considered 14 additional systems AGN–non-AGN from the literature and compare the total of 33 (14 + 19) systems with a sample of *bona fide* dual AGNs (De Rosa et al. 2018). Dual AGNs at separations larger than 10 kpc exhibit on the average a larger nuclear obscuration by about one order of magnitude with respect to the AGN/no-AGN systems (cf. Fig. 6);

(vii) galaxy pairs including *at least* an AGN exhibit a fraction of obscured nuclear activity larger than 70 per cent. This exceeds by a factor 1.5 the fraction of obscured objects in a sample of isolated AGNs of matching luminosities and redshifts (Ricci et al. 2015).

While this is suggestive that the galactic environment has a key influence on the AGN triggering in merging galaxies, deeper studies with a larger number of objects would be needed in order to perform a more quantitative comparison with the X-ray predictions of hydrodynamic simulations (Capelo et al. 2015, 2017). We aim at continuing these studies in the future (De Rosa et al. 2019).

ACKNOWLEDGEMENTS

The authors thank an anonymous referee, whose careful revision of the manuscript significantly improved the paper. We thank G. Calderone for help with QSFit. SB, ADR, and EP acknowledge financial support from the Italian Space Agency under grant ASI-INAF 2017-14-H.O. MPT acknowledges support from the Spanish MCIU through grant PGC2018-098915-B-C21 cofunded with FEDER funds and from the State Agency for Research of the Spanish MCIU through the 'Center of Excellence Severo Ochoa' award for the Instituto de Astrofísica de Andalucía (SEV-2017-0709) and through grant PGC2018-098915-B-C21 (MCI/AEI/FEDER, UE). Funding for SDSS-III has been provided by the Alfred P. Sloan Foundation, the Participating Institutions, the National Science Foundation, and the U.S. Department of Energy Office of Science. The SDSS-III web site is http://www.sdss3.org/. SDSS-III is managed by the Astrophysical Research Consortium for the Participating Institutions of the SDSS-III Collaboration including the University of Arizona, the Brazilian Participation Group, Brookhaven National Laboratory, Carnegie Mellon University, University of Florida, the French Participation Group, the German Participation Group, Harvard University, the Instituto de Astrofisica de Canarias, the Michigan State/Notre Dame/JINA Participation Group, Johns Hopkins University, Lawrence Berkeley National Laboratory, Max Planck Institute for Astrophysics, Max Planck Institute for Extraterrestrial Physics, New Mexico State University, New York University, Ohio State University, Pennsylvania State University, University of Portsmouth, Princeton University, the Spanish Participation Group, University of Tokyo, University of Utah, Vanderbilt University, University of Virginia, University of Washington, and Yale University.

DATA AVAILABILITY STATEMENT

The high-level data underlying this article are extracted through standard processing from raw data stored in public archives (SDSS and *XMM–Newton*), and will be shared on reasonable request to the corresponding author.

REFERENCES

Alam S. et al., 2015, ApJS, 219, 12
Alexander D. M., Hickox R. C., 2012, New Astron. Rev., 56, 93
Baldwin J. A., Phillips M. M., Terlevich R., 1981, PASP, 93, 5
Bassani L., Dadina M., Maiolino R., Salvati M., Risaliti G., Della Ceca R., Matt G., Zamorani G., 1999, ApJS, 121, 473
Begelman M. C., Volonteri M., Rees M. J., 2006, MNRAS, 370, 289
Bianchi S., Chiaberge M., Piconcelli E., Guainazzi M., Matt G., 2008, MNRAS, 386, 105
Bianchi S., Guainazzi M., Laor A., Stern J., Behar E., 2019, MNRAS, 485, 416
Blecha L. et al., 2016, MNRAS, 456, 961
Blecha L., Snyder G. F., Satyapal S., Ellison S. L., 2018, MNRAS, 478, 3056
Calderone G., Nicastro L., Ghisellini G., Dotti M., Sbarrato T., Shankar F., Colpi M., 2017, MNRAS, 472, 4051
Capelo P. R., Volonteri M., Dotti M., Bellovary J. M., Mayer L., Governato F., 2015, MNRAS, 447, 2123
Capelo P. R., Dotti M., Volonteri M., Mayer L., Bellovary J. M., Shen S., 2017, MNRAS, 469, 4437
Cardelli J. A., Clayton G. C., Mathis J. S., 1989, ApJ, 345, 245
Cash W., 1976, A&A, 52, 307

Condon J. J., Cotton W. D., Greisen E. W., Yin Q. F., Perley R. A., Taylor G. B., Broderick J. J., 1998, AJ, 115, 1693
Cruddace R. G., Hasinger G. H., Schmitt J. H., 1988, in Murtagh F., Heck A., Benvenuti P., eds, European Southern Observatory Conference and Workshop Proceedings Vol. 28, European Southern Observatory Conference and Workshop Proceedings, p. 177
Crummy J., Fabian A. C., Gallo L., Ross R. R., 2006, MNRAS, 365, 1067
De Rosa A. et al., 2018, MNRAS, 480, 1639
De Rosa A. et al., 2019, New Astron. Rev., 86, 101525
Di Matteo T., Springel V., Hernquist L., 2005, Nature, 433, 604
Done C., Davis S. W., Jin C., Blaes O., Ward M., 2012, MNRAS, 420, 1848
Ellison S. L., Patton D. R., Mendel J. T., Scudder J. M., 2011, MNRAS, 418, 2043
Fabian A. C. et al., 2009, Nature, 459, 540
Ferrarese L., Merritt D., 2000, ApJ, 539, L9
Gabriel C. et al., 2004, in Ochsenbein F., Allen M. G., Egret D., eds, ASP Conf. Ser. Vol. 314, Astronomical Data Analysis Software and Systems (ADASS) XIII. Astron. Soc. Pac., San Francisco, p. 759
Green P. J. et al., 2011, ApJ, 743, 81
Gross A. C., Fu H., Myers A. D., Wrobel J. M., Djorgovski S. G., 2019, ApJ, 883, 50
Guainazzi M., Bianchi S., 2007, MNRAS, 374, 1290
Guainazzi M., Piconcelli E., Jiménez-Bailón E., Matt G., 2005, A&A, 429, L9
Heckman T. M., Ptak A., Hornschemeier A., Kauffmann G., 2005, ApJ, 634, 161
Helfand D. J., White R. L., Becker R. H., 2015, ApJ, 801, 26
Hou M., Li Z., Liu X., 2020, ApJ, 900, 22
Hou M., Liu X., Guo H., Li Z., Shen Y., Green P. J., 2019, ApJ, 882, 41
Husemann B., Heidt J., De Rosa A., Vignali C., Bianchi S., Bogdanović T., Komossa S., Paragi Z., 2020, A&A, 639, A117
Imanishi M., Saito Y., 2014, ApJ, 780, 106
Iwasawa K. U V., Mazzarella J. M., Medling A. M., Sanders D. B., Evans A. S., 2018, A&A, 611, A71
Jansen F. et al., 2001, A&A, 365, L1
Kaastra J. S., 2017, A&A, 605, A51
Kaastra J. S., Bleeker J. A. M., 2016, A&A, 587, A151
Kauffmann G., Haehnelt M., 2000, MNRAS, 311, 576
Kewley L. J., Groves B., Kauffmann G., Heckman T., 2006, MNRAS, 372, 961
Kinkhabwala A. et al., 2002, ApJ, 575, 732
Kormendy J., Ho L. C., 2013, ARA&A, 51, 511
Koss M. et al., 2011, ApJ, 735, L42
Koss M. J. et al., 2018, Nature, 563, 214
Koss M., Mushotzky R., Treister E., Veilleux S., Vasudevan R., Trippe M., 2012, ApJ, 746, L22
Lamastra A., Bianchi S., Matt G., Perola G. C., Barcons X., Carrera F. J., 2009, A&A, 504, 73
McConnell N. J., Ma C.-P., 2013, ApJ, 764, 184
Magdziarz P., Zdziarski A. A., 1995, MNRAS, 273, 837
Marinucci A., Bianchi S., Nicastro F., Matt G., Goulding A. D., 2012, ApJ, 748, 130
Mayer L., Kazantzidis S., Escala A., Callegari S., 2010, Nature, 466, 1082
Middei R., Bianchi S., Marinucci A., Matt G., Petrucci P. O., Tamborra F., Tortosa A., 2019, A&A, 630, A131
Mulchaey J. S., Koratkar A., Ward M. J., Wilson A. S., Whittle M., Antonucci R. R. J., Kinney A. L., Hurt T., 1994, ApJ, 436, 586
Murphy K. D., Yaqoob T., 2009, MNRAS, 397, 1549
Osterbrock D. E., Ferland G. J., 2006, Astrophysics of Gaseous Nebulae and Active Galactic Nuclei. University Science Books, Sausalito, CA
Panessa F., Barcons X., Bassani L., Cappi M., Carrera F. J., Ho L. C., Pellegrini S., 2007, A&A, 467, 519
Pfeifle R. W. et al., 2019, ApJ, 875, 117
Piconcelli E. et al., 2010, ApJ, 722, L147
Protassov R., van Dyk D. A., Connors A., Kashyap V. L., Siemiginowska A., 2002, ApJ, 571, 545
Ranalli P., Comastri A., Setti G., 2003, A&A, 399, 39
Ricci C. et al., 2017, MNRAS, 468, 1273
Ricci C., Ueda Y., Koss M. J., Trakhtenbrot B., Bauer F. E., Gandhi P., 2015, ApJ, 815, L13
Rosen S. R. et al., 2016, A&A, 590, A1
Satyapal S. et al., 2017, ApJ, 848, 126
Satyapal S., Ellison S. L., McAlpine W., Hickox R. C., Patton D. R., Mendel J. T., 2014, MNRAS, 441, 1297
Silverman J. D. et al., 2011, ApJ, 743, 2
Smith R. K., Brickhouse N. S., Liedahl D. A., Raymond J. C., 2001, ApJ, 556, L91
Steinborn L. K., Dolag K., Comerford J. M., Hirschmann M., Remus R.-S., Teklu A. F., 2016, MNRAS, 458, 1013
Stern D. et al., 2012, ApJ, 753, 30
Strüder L. et al., 2001, A&A, 365, L18
Tortosa A., Bianchi S., Marinucci A., Matt G., Petrucci P. O., 2018, A&A, 614, A37
Turner M. J. L. et al., 2001, A&A, 365, L27
Van Wassenhove S., Volonteri M., Mayer L., Dotti M., Bellovary J., Callegari S., 2012, ApJ, 748, L7
Vignali C., Alexander D. M., Gilli R., Pozzi F., 2010, MNRAS, 404, 48
Volonteri M., Dubois Y., Pichon C., Devriendt J., 2016, MNRAS, 460, 2979
Weston M. E., McIntosh D. H., Brodwin M., Mann J., Cooper A., McConnell A., Nielsen J. L., 2017, MNRAS, 464, 3882

APPENDIX A: *XMM–NEWTON*/EPIC SPECTRA OF *BONA FIDE* AGN

In Figs A1 and A2, we show the EPIC spectra, best-fitting model (upper panels), and residuals against the best-fitting model in units of data/model ratio for the 19 *bona fide* AGNs in our sample. Each data point corresponds to a signal-to-noise ratio larger than three.

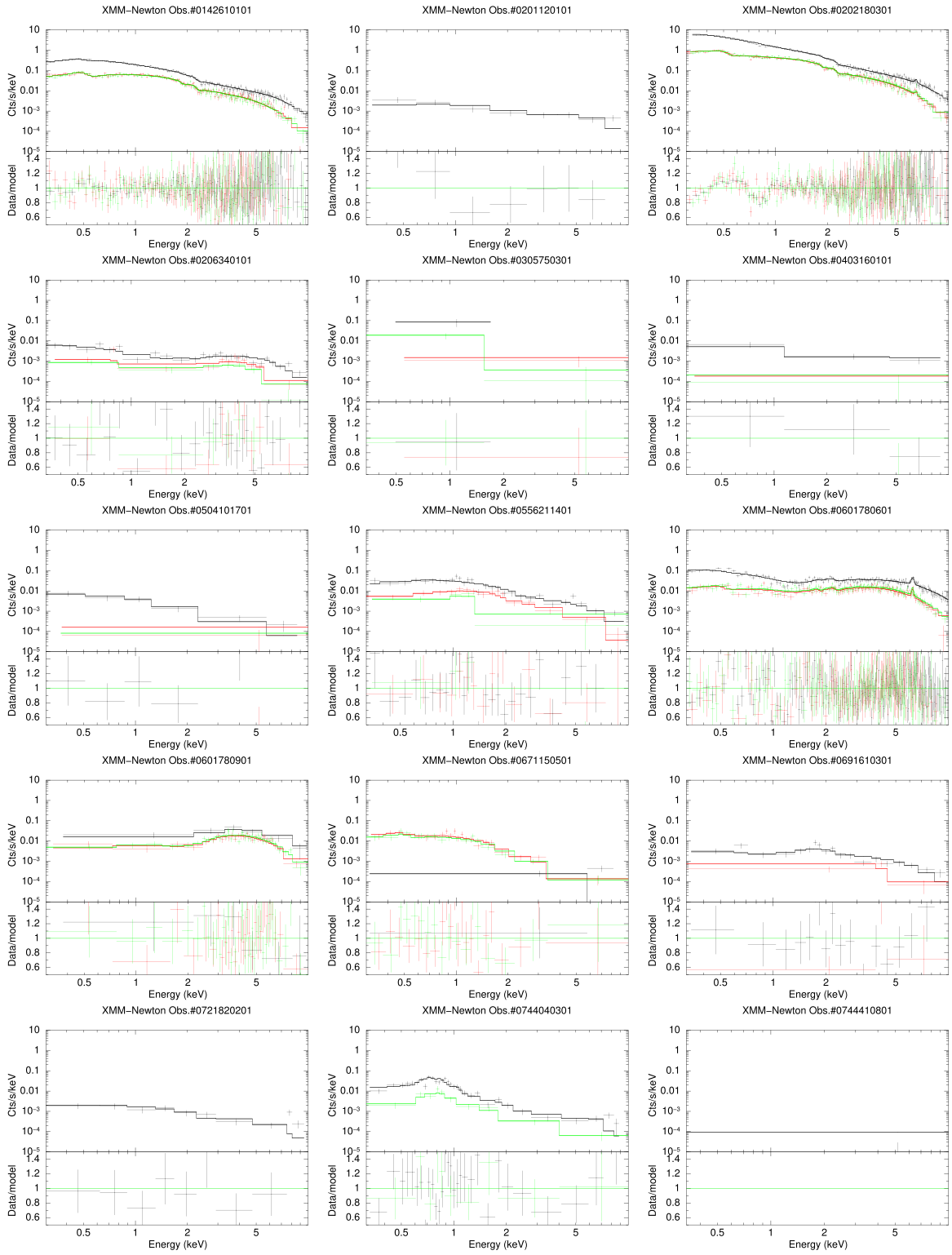

Figure A1. Upper panels: EPIC spectra (crosses) and best-fitting models (solid lines) for the 19 bona fide AGN spectra in our sample. Lower panels: residuals against the best-fitting model in units of data/model ratio. Black: EPIC-pn; red: EPIC-MOS1; green: EPIC-MOS2. Each data point corresponds to a minimum signal-to-noise ratio ≥3.

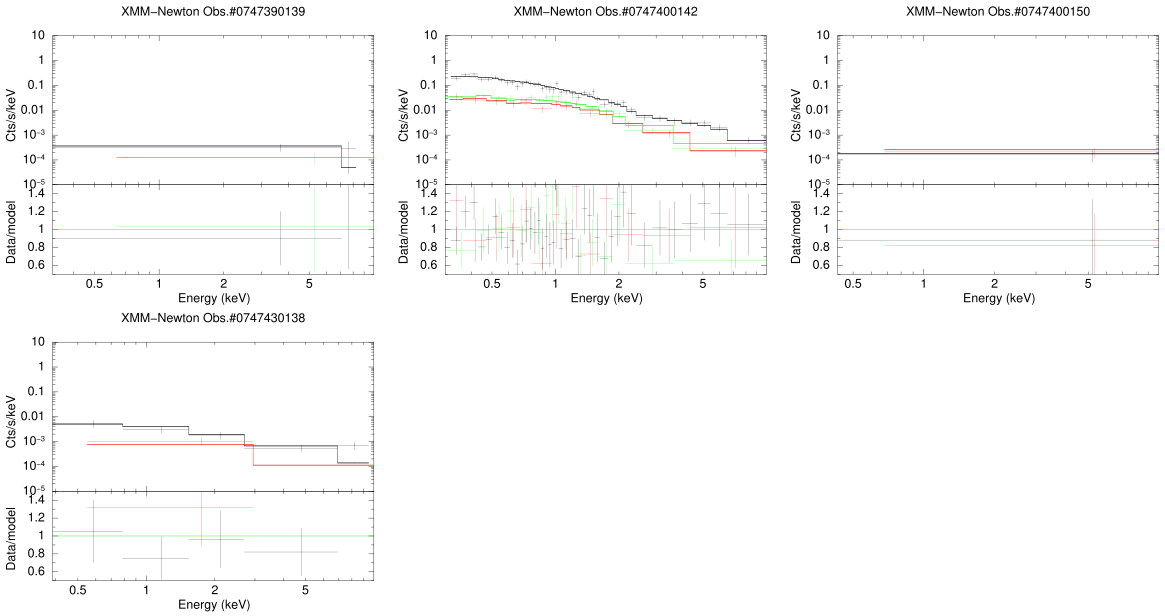

Figure A2. Continuation of Fig. A1.

This paper has been typeset from a TEX/LATEX file prepared by the author.